CrossMark

Casting Light on Degeneracies: A Comprehensive Study of Lightcurve Variations in Microlensing Events OGLE-2017-BLG-0103 and OGLE-2017-BLG-0192

Sarang Shah
Indian Institute of Astrophysics, Koramangala, Bengaluru, 560034, India; sshah1502@gmail.com
Received 2023 December 30; revised 2024 July 10; accepted 2024 August 6; published 2024 September 27

Abstract

This study investigates orbital parallax in gravitational microlensing events, focusing on OGLE-2017-BLG-0103 and OGLE-2017-BLG-0192. For events with timescales $\leqslant$60 days, a Jerk-Parallax degeneracy arises due to high Jerk velocity ($\tilde{v}_j$), causing a fourfold continuous parallax degeneracy. OGLE-2017-BLG-0103, after incorporating orbital parallax, reveals four discrete degenerate parallax solutions, while OGLE-2017-BLG-0192 exhibits four discrete solutions without degeneracy. The asymmetric lightcurve of OGLE-2017-BLG-0103 suggests a more probable model where Xallarap is added to the parallax model, introducing tension. The galactic model analysis predicts a very low-mass stellar lens for OGLE-2017-BLG-0192. For OGLE-2017-BLG-0103, degenerate solutions suggest a low-mass star or a darker lens in the disk, while the Xallarap+Parallax model also predicts a stellar lens in the bulge, with the source being a solar-type star orbited by a dwarf star. This study presents five degenerate solutions for OGLE-2017-BLG-0103, emphasizing the potential for confirmation through high-resolution Adaptive Optics observations with Extremely Large Telescopes in the future. The complexities of degenerate scenarios in these microlensing events underscore the need to analyze special single-lens events in the Roman Telescope Era.

Unified Astronomy Thesaurus concepts: Binary source microlensing (2141); Gravitational microlensing (672); Microlensing parallax (2144)

1. Introduction

Gravitational microlensing (A. Einstein 1936; B. Paczynski 1986) is an intriguing astronomical phenomenon where the gravity of a foreground lens causes the light from a background source to bend, resulting in the appearance of multiple images when their relative proximity in the sky is closer than the θ_E, which is given by

$$\theta_E = \sqrt{\frac{4GM_L}{c^2}\left(\frac{1}{D_L} - \frac{1}{D_S}\right)} \qquad (1)$$

where $4G/c^2 \sim 8.14$ mas $M_\odot^{-1}$, M_L is the mass of the lens, and D_L and D_S are the distances to the lens and source, respectively. These images are not individually resolved, distinguishing microlensing from Gravitational Lensing. Instead, microlensing is detectable as a temporary fluctuation in the brightness of the source star when continuously observed over days or months. This phenomenon produces a characteristic lightcurve known as the Paczynski curve (B. Paczynski 1986) when plotted over time. It was only through the establishment of dedicated survey groups such as OGLE-I (A. Udalski et al. 1994), EROS (E. Aubourg et al. 1993), and MACHO (C. Alcock et al. 1993) that the first microlensing event toward the galactic bulge was observed (C. Alcock et al. 1995a, 1995b). Since then, this field has rapidly expanded, shedding light on the mysteries of the inner Milky Way, thanks to the latest generation of survey telescopes like OGLE-IV (A. Udalski et al. 2015), KMTNet (S.-L. Kim et al. 2016), and MOA-III (I. A. Bond et al. 2001; T. Sumi et al. 2003) equipped with a wide-field camera.

A straightforward way to parameterize a microlensing event is to consider a point lens, a point source, and the observer-lens-source combination moving in relative motion. In such a scenario, the separation between the lens and the source, normalized to the angular Einstein radius of the lens, is given by

$$u(t) = \sqrt{u_0^2 + \left(\frac{t - t_0}{t_E}\right)^2}. \qquad (2)$$

Here, $u(t)$ is a function of time t, u_0 and t_0 represent the impact parameters and the time of the closest approach, and t_E corresponds to the time the source takes to cross the Einstein Radius. The time-varying magnification is then given by

$$A(t) = \frac{u^2 + 2}{u\sqrt{u^2 + 4}}. \qquad (3)$$

Although the lens itself cannot be directly detected during a microlensing event, higher-order effects can sometimes be observed, leading to the characterization of the lens. One such effect is known as Microlensing Parallax (π_E), which is a vector quantity having a magnitude equal to $\tilde{r}_E$ and a direction similar to the project lens-source proper motion (μ_{rel}) (Equation (4)). Orbital parallax causes the source to follow a nonrectilinear trajectory, resulting in an asymmetric lightcurve, which becomes significant for events lasting 60 days or longer (A. Gould et al. 1994; C. Alcock et al. 1995a; I. Soszynski et al. 2001; D. P. Bennett et al. 2002a, 2002b; I. A. Bond et al. 2002; S. Mao et al. 2002; M. C. Smith 2003). During this period, the Earth's displacement around the Sun is approximately 1.03 au (see Figure 1). The typical value of $\tilde{r}_E$ for M-dwarf lenses toward the bulge is around 2 au, which, while larger, is comparable to the chord length depicted in Figure 1. For events with shorter timescales (t_E), the chord length is much smaller
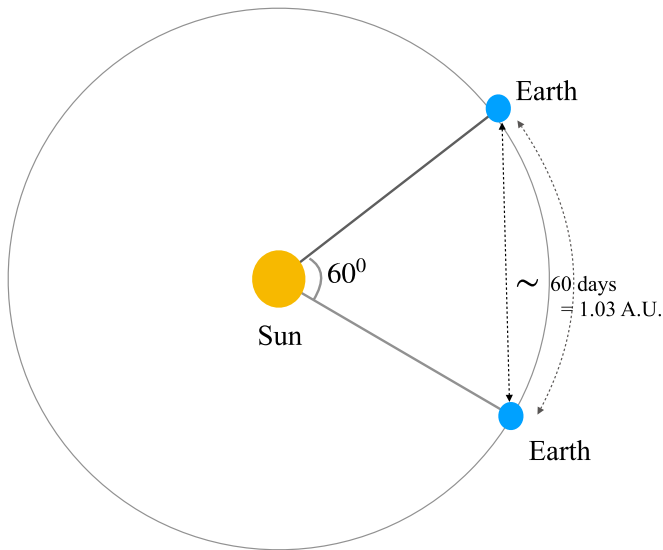
Figure 1. The projected r_E for the lenses toward the bulge on the ecliptic plane is ∼1.03 au. Earth also displaces by this value in 60 days. The displacement equal to the projected Einstein radius of the lens helps to measure the orbital parallax.

than 1.03 au, rendering π_E unconstrained due to negligible perturbations in the lightcurve. However, for longer-duration events where the displacement exceeds the chord length, π_E can be effectively constrained, resulting in a noticeably asymmetric lightcurve. Alternatively, even if the timescale of an event is larger than 60 days, but the lens has a low mass, then the value of $\tilde{r}_E$ will be smaller, and hence the π_E won't be constrained properly, eventually leading to degenerate solutions.

$$\pi_E = \frac{1}{\tilde{r}_E}\text{au}. \quad (4)$$

Note that the π_E is a vector quantity and the direction of the π_E vector is similar to the direction of the lens-source proper motion ($\boldsymbol{\mu}_{\text{rel}} = \boldsymbol{\theta}_E/t_E$) vector (A. Gould 1992). Then, the mass of the lens can be calculated using

$$M_L = \frac{\pi_{\text{rel}}}{\kappa \pi_E^2} = \frac{\theta_E}{\kappa \pi_E} \quad (5)$$

where $\pi_{\text{rel}} = \text{au}\left(\frac{1}{D_L} - \frac{1}{D_s}\right)$ is the relative lens-source parallax. So, the mass of the lens can be measured if we know the value of π_{rel} or θ_E in addition to π_E. Since the lens is usually faint and distant, we cannot measure D_L (and hence π_{rel}) directly. The parameter θ_E is also obtained from the lightcurve when finite-source effects are measured (see A. Gould 1994; R. J. Nemiroff & W. A. D. T. Wickramasinghe 1994; H. J. Witt & S. Mao 1995). Interestingly, only a handful of single-lens events have directly measured the value of θ_E either by measuring finite-source effects in extremely high magnification events (J. Yoo et al. 2004; A. Gould et al. 2009), via resolution of microlensing images using interferometry (F. Delplancke et al. 2001; S. Dong et al. 2019), or via astrometric microlensing (E. Hog et al. 1995; K. C. Sahu et al. 2022). As these measurements are not possible for every microlensing event, measuring π_E signatures in the lightcurve helps to put constraints on M_L and D_L.

For microlensing events having timescales ∼60 days, A. Gould (2004) showed that they suffer from a fourfold

continuous degeneracy called Jerk-Parallax (π_j) degeneracy. This degeneracy is important when the value of $\tilde{v}_j$ is high and t_E is ∼60 days. As t_E increases, the continuous degeneracy is broken into discrete degeneracy and completely broken for very long t_E events. We encourage the readers to refer M. C. Smith et al. (2003) and A. Gould (2004) to understand the origins and fundamentals of this degeneracy. While this degeneracy has been explored before by A. Gould (2004), B. -G. Park et al. (2004), G. Jiang et al. (2004), and S. Poindexter et al. (2005), exactly, how this degeneracy breaks as t_E increases and how multisite observations help in realizing this degeneracy has never been seen before. While the events analyzed by the first three authors had timescales $\leqslant$ 60 days, the latter found degenerate solutions in events having t_E higher than 60 days.

In this paper, we present our analysis of the microlensing events OGLE-2017-BLG-0103 and OGLE-2017-BLG-0192. By modeling the lightcurve involving π_E, we identify the existence of a discrete Jerk-Parallax degeneracy in the lightcurve of the former event but not later. We also explore the possibility of the source having an orbiting companion causing effects (also called Xallarap) similar to the observed orbital parallax effect. For OGLE-2017-BLG-0103, we find a strong degeneracy between the orbital parallax and the Xallarap +Parallax model. We do not find such tension in OGLE-2017-BLG-0192.

1.1. Overview

After an introduction, we discuss the details of the data used in this analysis in Section 2. In the initial part of Section 3, we describe the microlensing model that we use to fit the observed data followed by Subsections 3.1 and 3.2, where we talk about our approach to finding the Jerk-Parallax degenerate solutions (both giving similar results), followed by Section 3.3 where we discuss our Xallarap model. In Section 4, we analyze the source and the blend, which is followed by Section 5, where we obtain the distance to and mass of the lens. Finally, we discuss our results and conclude in Section 6.

2. Observations and Data Reductions

OGLE-2017-BLG-0103 is the 103rd event detected by the Early Warning System (EWS) of OGLE in the field BLG501.11, while OGLE-2017-BLG-0192 is the 192nd detected in the OGLE field BLG518.09. It was observed toward the galactic bulge through its 1.3 m Warsaw Telescope, located at the Las Campanas Observatory in Chile (A. Udalski et al. 2015). OGLE has a wide-field CCD camera, a mosaic of 32 2 k x 4 k individual chips. Together, they contribute to the camera having a wide field of view (FOV) of 1.4 deg². The calibrated source in both of these events is a faint star with a baseline magnitude of $I \geqslant 18.5$ mag on the OGLE photometric maps. The equatorial coordinates of OGLE-2017-BLG-0103 are $\alpha = 17:52:31.49$ and $\delta = -30:00:44.4$, which can be translated to galactic coordinates as $l = 359°85008$ and $b = -1°84077$. Similarly, the equatorial coordinates for OGLE-2017-BLG-0192 are $\alpha = 18:10:34.45$ and $\delta = -26:50:25.9$, which can be translated to $(l,b) = (4°57154°, -3°7277)$. We download the OGLE photometry for both events, which is available on its homepage. This photometry is generated after performing the difference image analysis of the field images that use the algorithm by C. Alard & R. H. Lupton (1998). Both of these microlensing
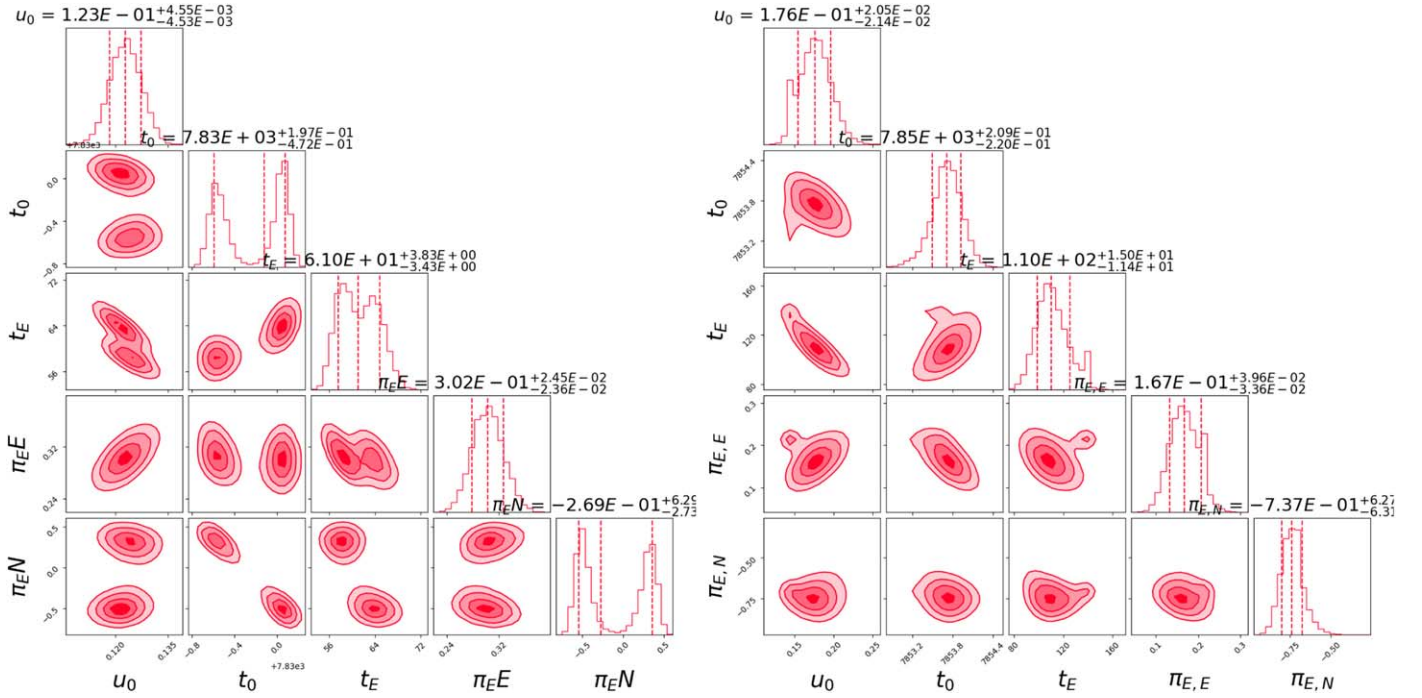
Figure 2. The covariance plots of the model parameters for OGLE-2017-BLG-0103 (left) and OGLE-2017-BLG-0192 (right). In the case of OGLE-2017-BLG-0103, we can see the Jerk-Parallax degeneracy in the bimodal distributions of π_{EN}, t_0, and t_E.

events were also observed independently by KMTNet through its three 1.8 m telescopes spread across longitude in the Southern Hemisphere in Chile (KMT-C), South Africa (KMT-S), and Australia (KMT-A). Both of these events were also found during the 2016 season by KMTNet's event finder algorithm (H. -W. Kim et al. 2018) and were designated in the KMTNet database as KMT-2017-BLG-1698 and KMT-2017-BLG-1225. All three KMTNet telescopes have 4 deg^2 wide-field cameras, each with four 9k x 9k chips to monitor the Galactic field (S.-L. Kim et al. 2016). While OGLE-2017-BLG-0103 was observed in two fields—BLG02 and BLG42—OGLE-2017-BLG-0192 was observed in the field BLG31 by the KMTNet. Most of the observations were taken in the I band; there are occasional V-band observations for these events. The KMTNet images in the I and V bands were reduced using the pyDIA software (Albrow 2017), based on difference image analysis using the delta-basis-function approach of D. M. Bramich et al. (2013).

3. Analysis

As mentioned in the introduction, a single-lens and single-source lightcurve is described by three Paczynski parameters: u_0, t_0, and t_E. Two additional fit parameters, the f_s and f_b, are the source and blend fluxes obtained by performing a linear fit of the model to the observed data (refer to Equation (6)). However, as we describe later, we incorporate a few additional parameters and form a higher-order model to fit the asymmetry in the data. We model the observed light-curve of both events using the I-band data of OGLE and KMTNet. So we have 14 and 8 values of f_s and f_b for OGLE-2017-BLG-0103 and OGLE-2017-BLG-0192, respectively, in addition to three Paczynski parameters to fit the observed lightcurve.

$$\text{Model}(t) = A(t)f_s + f_b. \qquad (6)$$

3.1. Orbital Parallax Model

The single-lens model did not fit the rising side of the asymmetric lightcurves of these events. So, we explore the orbital parallax model by adding two parameters π_{EE} and π_{EN}. We initially perform a coarse grid search minimizing χ^2 in the (π_{EE}, π_{EN}) plane by holding the Paczynski parameters constant. For OGLE-2017-BLG-0103, we found a minimum at (π_{EE}, π_{EN}) = (0.184, −0.168) and for OGLE-2017-BLG-0192 at (0.120, −0.392). We seed these parameters along with Paczynski parameters to *emcee* (D. Foreman-Mackey et al. 2013) and obtained a fitting model called P1. We then renormalized the photometric uncertainties in magnitudes using the P1 model so that χ^2/degrees of freedom (dof) ~ 1. After renormalizing the photometric uncertainties, the P1 model was rerun, which converged to a solution shown in Figure 2 where we see the Jerk-Parallax degeneracy in the discrete contours of the model parameters. Similarly, Figure 2 shows the P1-model parameter distributions for OGLE-2017-BLG-0192 where we do not see any bimodal distributions of the π_{EN}, t_E, and t_0 parameters, which indicates that the degeneracy is broken in this case.

For OGLE-2017-BLG-0103, we term the model corresponding to the left mode in the π_{EN} distribution as P3. To explore the mirrored degenerate solutions, which are also the ecliptic degenerate solutions, we seed the *emcee* with the P1 model but with the sign of u_0 reversed (see G. Jiang et al. 2004; S. Poindexter et al. 2005; J. Skowron et al. 2011). The walkers then converge to new solutions P2 and P4. Thus, we find all four degenerate solutions where P3 and P4 are the Jerk-Parallax degenerate solutions corresponding to P1 and P2, respectively. While P4 is the constant-acceleration degenerate pair of P3, it is the ecliptic degenerate counterpart of P1 (and similarly, P2 is the constant-acceleration pair of P1 and ecliptic degenerate P3). The trajectories for these pairs take the path shown in Figure 3. So, we must expect similar
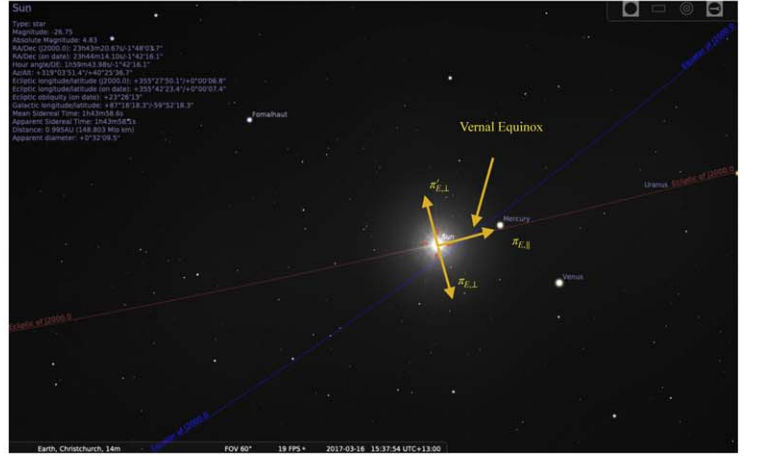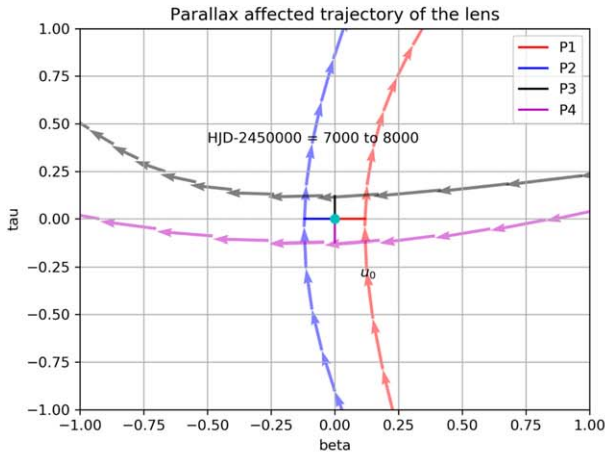
Figure 3. (a) shows different trajectories corresponding to the obtained Jerk-Parallax solutions. The red trajectory corresponds to P1, the blue corresponds to P2, the black corresponds to P3, and the magenta corresponds to P4. (b) a screenshot from Stellarium software shows the Sun's path projected in the plane of the sky during the OGLE-2017-BLG-103's peak. The Sun's projected acceleration is along the ecliptic toward the intersection of both planes. The jerk velocity is ~ 165.62 km s^{-1}.

lens properties for each pair of ecliptic degenerate solutions but different for the Jerk-Parallax degenerate solution. In Figure 3, we show the contours of π_E of all the solutions. Although we do not see any bimodal distributions in the case of OGLE-2017-BLG-0192, we still repeat the above procedure and find that the discrete solutions are not very far from each other in the π_E plane (see Figure 4).

3.2. Alternative Method to Find Jerk-Parallax Solutions

We show an alternative way to find the Jerk-Parallax degenerate solutions for the event OGLE-2017-BLG-0103 based on the framework by J. H. An et al. (2002), M. C. Smith et al. (2003), and A. Gould (2004) and also used by G. Jiang et al. (2004) and B. -G. Park et al. (2004). In this method, we find the Sun's celestial position at the event's peak and obtain the velocity ($v_\oplus$) and acceleration (α). At the time of the vernal equinox of the year 2017 (which was close to t_0 of OGLE-2017-BLG-0103), the acceleration of the Sun projected into the sky was

$$\alpha(n, e) = (-2.44 \times 10^{-7}, 1.49 \times 10^{-4}) \text{ Km day}^{-2}.$$

The projected acceleration points $359°.80$ north through east in the sky. Since the parallax contours are elongated in the direction perpendicular to this direction at $269°.9$, to find the model P3, we first find $\pi_{E,\parallel}$ and $\pi_{E,\perp}$, the components of π_E parallel and perpendicular to the acceleration of the Sun in the sky at $\sim(0.43, 0.00)$, respectively. Then, the perpendicular component of the degenerate parallax solution is found by using the relation

$$\pi'_{E,\perp} = -(\pi_{E,\perp} + \pi_{j,\perp}) \tag{7}$$

where $\pi_{j,\perp}$ is the perpendicular component of the Jerk-Parallax and is calculated by

$$\pi_{j,\perp} = -\frac{4}{3} \frac{1\text{yr}}{2\pi t_E} \frac{\sin\beta_{ecl}}{(\cos^2\psi\sin^2\beta_{ecl} + \sin^2\psi)^{3/2}} \tag{8}$$

where β_{ecl} is the ecliptic latitude of the event and ψ is the phase of the Earth's orbit. Using Equation (8), we get $\pi_{j,\perp} = 0.17$. Thus, the location of the degenerate parallax solution is $(\pi'_{E,\parallel}, \pi'_{E,\perp}) = (0.43, -0.17)$. The Sun's path in the plane of the

sky can be visualized in Figure 3 where the background image is a screenshot of Stellarium v.0.15.1[1] and the ecliptic and equatorial planes are shown in red and blue colors, respectively. We can also see the projected position of the Sun close to the vernal equinox, the direction of projected acceleration toward the intersection of the ecliptic and equatorial planes. There is one component of π_E parallel to the acceleration along the ecliptic and two antiparallel perpendicular components causing this degeneracy.

In Figure 4, we see that the major axes of the elliptical covariances in the first plot for OGLE are nearly perpendicular to each other. Since the direction of π_E is the direction of μ_{rel} in the adopted frame of reference, the direction of μ_{rel} for P3 will be perpendicular to the direction of μ_{rel} in the P1 solution (see Figure 3). As the direction of μ_{rel} for the P1 solution is $\arctan(\pi_{EN}/\pi_{EE}) = 47°$, the direction of μ_{rel} for the P3 solution should be $137°$. Thus, we can convert $(\pi_{E,\parallel}, \pi_{E,\perp}')$ derived earlier to celestial frame $(\pi_{EE}, \pi_{EN}) = (0.30, -0.34)$ using J. H. An et al. (2002). After seeding *emcee* with the Paczynski parameters of the P1 solution and these parallax parameters, we found that the median value of the degenerate parallax parameters is $(\pi_{EE}, \pi_{EN}) = (0.30, -0.50)$. Furthermore, t_0 and t_E also converge to the other mode of the bimodal distribution of the samples. Similarly, the other P4 solution was found using the P2 solution. In all the solutions, it is observed that $\pi_{E,\parallel} > \pi_{E,\perp}$[2], which is also seen in the lightcurve. The samples of the model parameters corresponding to each solution with their 16th, 50th, and 84th percentile values are shown in Table 1. Similarly, the model parameters for the different parallax solutions with their 16th, 50th, and 84th percentile values for OGLE-2017-BLG-0192 are shown in Table 2 and the lightcurve in Figure 5.

3.3. Xallarap Effect

Like the motion of the Earth around the Sun, a companion orbiting to the source might also cause similar perturbations in the lightcurve due to orbital parallax (K. Griest & W. Hu 1992;

---

[1] www.stellarium.org

[2] $\pi_{E,\parallel}$ is responsible for the asymmetry about the base in the lightcurve. In contrast, $\pi_{E,\perp}$ is responsible for the asymmetry about the peak of the lightcurve.
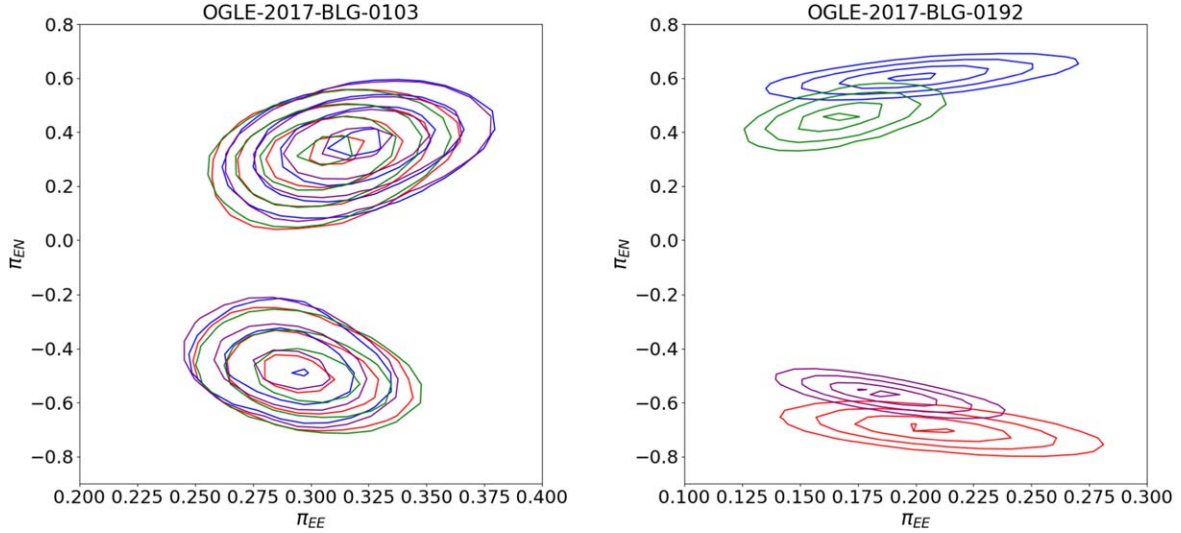
Figure 4. In the first plot, the fit to the lightcurve with the orbital parallax model is red, while the black dotted model represents a Paczynski Curve. The other two plots are the triangle plots showing the degenerate solutions. The right mode of the bimodal distribution of π_{EN}, t_E, and t_0 in the center plot shows the P1 model, while the corresponding Jerk-Parallax model P3 is the left mode. Similarly, the solution P4 is the one that corresponds to the left mode of the bimodal distribution of π_{EN}, t_E, and t_0, while P2 is on the right. (P1, P2) and (P3, P4) are related by the *ecliptic* degeneracy.

Table 1
The Table Shows the Parameter Means and Uncertainties Corresponding to Each Degenerate π_E Solution for the Event OGLE-2017-BLG-0103

			Microlensing Model Results				
Parameter	PSPL	P1	P2	P3	P4	Xallarap	Xallarap+Parallax
χ^2	49123.42	11288.62	11290.50	11289.86	11290.90	11282.85	11237.26
u_0	0.099 ± 0.001	0.123 ± 0.001	-0.122 ± 0.001	0.123 ± 0.001	-0.123 ± 0.001	0.104 ± 0.09	$-0.144^{+0.006}_{0.008}$
t_0 (days)	7829.90 ± 0.01	7829.44 ± 0.09	7829.67 ± 0.03	7830.05 ± 0.06	7829.67 ± 0.03	7829.66 ± 0.06	7830.37 ± 0.04
t_E (days)	73.12 ± 0.01	58.26 ± 1.62	60.42 ± 2.12	63.91 ± 2.22	60.23 ± 2.06	73.17 ± 3.22	53.63 ± 2.07
$\pi_{E,E}$	$\cdots$	0.31 ± 0.02	0.30 ± 0.02	0.30 ± 0.02	0.30 ± 0.02	$\cdots$	-0.014 ± 0.004
$\pi_{E,N}$	$\cdots$	0.32 ± 0.08	-0.02 ± 0.41	-0.50 ± 0.11	0.02 ± 0.40	$\cdots$	0.002 ± 0.002
ξ_1	$\cdots$	$\cdots$	$\cdots$	$\cdots$	$\cdots$	-0.001 ± 0.002	0.001 ± 0.001
ξ_2	$\cdots$	$\cdots$	$\cdots$	$\cdots$	$\cdots$	4.28 ± 1.22	$0.16^{+0.02}_{-0.01}$
ω	$\cdots$	$\cdots$	$\cdots$	$\cdots$	$\cdots$	0.004 ± 0.001	0.024 ± 0.02
i	$\cdots$	$\cdots$	$\cdots$	$\cdots$	$\cdots$	1.56 ± 0.02	1.56 ± 0.01
ϕ_0	$\cdots$	$\cdots$	$\cdots$	$\cdots$	$\cdots$	1.42 ± 0.14	1.74 ± 0.19
q_s	$\cdots$	$\cdots$	$\cdots$	$\cdots$	$\cdots$	0.0	$0.51^{+0.03}_{-0.04}$
$f_{s,\text{OGLE}}$	2135.62 ± 7.45	2142.26 ± 8.57	2142.10 ± 8.57	2139.82 ± 3.21	2159.93 ± 8.64	2140.78 ± 9.32	2140.78 ± 9.32
$f_{s,\text{KMTA31}}$	1565.32 ± 9.80	1570.63 ± 11.40	1571.00 ± 11.41	1568.81 ± 5.49	1584.84 ± 11.51	1570.67 ± 11.12	1570.67 ± 11.12
$f_{s,\text{KMTC31}}$	2275.56 ± 4.26	2323.37 ± 4.53	2323.60 ± 4.53	2321.11 ± 7.97	2343.57 ± 9.12	2321.25 ± 4.62	2321.25 ± 4.62
$f_{s,\text{KMTS31}}$	2127.67 ± 7.38	2125.29 ± 7.37	2125.41 ± 7.37	2123.11 ± 7.37	2143.57 ± 7.44	2124.68 ± 7.03	2124.68 ± 7.03
$f_{s,\text{KMTA42}}$	1570.51 ± 6.97	1578.11 ± 7.98	1578.17 ± 7.98	1575.87 ± 4.52	1591.36 ± 8.04	1576.63 ± 7.99	1576.63 ± 7.99
$f_{s,\text{KMTC42}}$	2342.34 ± 4.57	2323.30 ± 5.49	2323.09 ± 5.49	2320.80 ± 11.39	2342.46 ± 5.54	2322.00 ± 5.30	2322.00 ± 5.30
$f_{s,\text{KMTS42}}$	2126.89 ± 5.67	2125.77 ± 5.84	2125.38 ± 5.84	2123.36 ± 8.56	2143.01 ± 5.89	2126.87 ± 6.32	2126.87 ± 6.32
$f_{b,\text{OGLE}}$	1801.27 ± 21.88	1803.28 ± 22.81	1810.18 ± 22.83	1811.93 ± 22.80	1800.28 ± 22.84	1801.21 ± 22.43	1563.44 ± 72.43
$f_{b,\text{KMTA31}}$	2749.22 ± 11.20	2747.28 ± 11.43	2750.22 ± 18.63	2752.91 ± 11.43	2740.65 ± 11.51	2745.24 ± 12.21	2495.24 ± 180.21
$f_{b,\text{KMTC31}}$	2212.63 ± 18.97	2213.61 ± 19.18	2219.03 ± 9.12	2221.69 ± 19.18	2205.86 ± 4.57	2745.24 ± 12.21	1833.24 ± 128.21
$f_{b,\text{KMTS31}}$	12200.56 ± 16.03	12177.35 ± 15.99	12182.79 ± 16.01	12185.16 ± 15.99	12171.50 ± 19.22	12177.73 ± 16.78	11848.73 ± 316.78
$f_{b,\text{KMTA42}}$	2735.54 ± 9.30	2738.75 ± 9.10	2743.07 ± 19.21	2745.75 ± 9.10	2735.71 ± 8.04	2736.98 ± 9.12	2519.98 ± 179.12
$f_{b,\text{KMTC42}}$	2176.66 ± 15.98	2177.66 ± 18.60	2184.12 ± 13.92	2186.66 ± 18.60	2174.00 ± 5.54	2176.76 ± 17.76	1816.76 ± 127.76
$f_{b,\text{KMTS42}}$	12175.72 ± 24.30	12172.96 ± 22.80	12180.16 ± 22.83	12181.64 ± 22.80	12170.82 ± 22.84	12175.96 ± 25.40	11859.96 ± 325.40

Note. The corresponding linear-fit parameters source flux (f_s) and the blend flux (f_b) with their uncertainties are also shown.

B. Paczynski 1997; M. Dominik 1998; M. C. Smith et al. 2003). When the orbital effect is insignificant, the lightcurve of a binary-source event can be assumed as the superposition of the lightcurves of static individual sources. Conversely, in cases where the orbital effect is substantial, it necessitates the incorporation of the orbital dynamics. The study of binary sources and their orbital motion in microlensing lightcurves may even provide new opportunities: it may help break degeneracies in microlensing (K. Griest & W. Hu 1992; B. Paczynski 1997; C. Han & A. Gould 1997), or it may open a new channel to discover planets orbiting around the source star (S. Rahvar & M. Dominik 2009; F. Bagheri et al. 2019; S. Miyazaki et al. 2021). The periods of binary systems may range from a few hours for very close systems to hundreds of

<div align="center">

Table 2

The Table Shows the Parameter Means and Uncertainties Corresponding to the Fitted Orbital Parallax and Xallarap Model of OGLE-2017-BLG-0192

</div>

			Microlensing Model Results			
Parameter	PSPL	P1	P2	P3	P4	Xallarap
χ^2	4810.66	1540.73	1548.62	1581.93	1568.16	1636.83
u_0	0.134 ± 0.005	0.14 ± 0.02	-0.10 ± 0.02	0.08 ± 0.02	-0.11 ± 0.02	$-0.14^{+0.06}_{-0.07}$
t_0 (days)	7853.78 ± 0.06	7853.69 ± 0.19	7853.33 ± 0.19	7850.52 ± 0.39	7851.31 ± 0.29	7830.12 ± 0.25
t_E (days)	122.70 ± 0.06	139.97 ± 22.16	196.42 ± 41.39	175.93 ± 30.66	137.01 ± 21.00	$72.90^{+4.06}_{-5.90}$
$\pi_{E,E}$	$\cdots$	0.21 ± 0.03	0.20 ± 0.03	0.17 ± 0.02	0.19 ± 0.02	$\cdots$
$\pi_{E,N}$	$\cdots$	-0.70 ± 0.05	0.61 ± 0.04	0.46 ± 0.04	-0.57 ± 0.04	$\cdots$
ξ_1	$\cdots$	$\cdots$	$\cdots$	$\cdots$	$\cdots$	0.0002 ± 0.0001
ξ_2	$\cdots$	$\cdots$	$\cdots$	$\cdots$	$\cdots$	$2.36^{+0.58}_{-3.40}$
ω	$\cdots$	$\cdots$	$\cdots$	$\cdots$	$\cdots$	0.0048 ± 0.0008
i	$\cdots$	$\cdots$	$\cdots$	$\cdots$	$\cdots$	1.571 ± 0.001
ϕ_0	$\cdots$	$\cdots$	$\cdots$	$\cdots$	$\cdots$	$2.01^{+0.24}_{-1.47}$
$\log(q_s)$	$\cdots$	$\cdots$	$\cdots$	$\cdots$	$\cdots$	$-2.88^{+5.57}_{-4.79}$
$f_{s,\text{OGLE}}$	1373.28 ± 5.88	1374.07 ± 6.00	1371.29 ± 6.01	1372.89 ± 6.00	1373.28 ± 6.02	2949.99 ± 14.70
$f_{s,\text{KMTA02}}$	19738.09 ± 311.20	19737.93 ± 316.31	19732.00 ± 318.63	19735.91 ± 312.43	19735.65 ± 311.51	35827.25 ± 150.20
$f_{s,\text{KMTC02}}$	11618.32 ± 102.97	11615.34 ± 102.09	11609.99 ± 103.12	11612.32 ± 103.18	11612.86 ± 102.57	21038.56 ± 198.67
$f_{s,\text{KMTS02}}$	23098.56 ± 191.52	23099.35 ± 190.98	23104.18 ± 196.01	23085.16 ± 195.99	23071.50 ± 193.22	42085.30 ± 22.08
$f_{b,\text{OGLE}}$	1308.62 ± 12.45	1308.13 ± 12.37	1306.06 ± 8.57	1306.53 ± 6.21	1309.65 ± 7.64	-284.13 ± 7.89
$f_{b,\text{KMTA02}}$	15652.32 ± 653.80	15648.00 ± 653.16	15711.00 ± 614.41	15648.81 ± 648.49	15804.84 ± 611.51	126.39 ± 4.56
$f_{b,\text{KMTC02}}$	13201.72 ± 294.26	13156.13 ± 293.72	13178.62 ± 288.58	13165.11 ± 297.97	13149.57 ± 290.12	4229.28 ± 38.32
$f_{b,\text{KMTS02}}$	18078.63 ± 460.59	18077.67 ± 467.27	18069.81 ± 480.01	18075.00 ± 477.37	18070.00 ± 467.44	159.63 ± 7.79

Note. The corresponding linear-fit parameters source flux (f_s) and the blend flux (f_b) with their uncertainties are also shown.
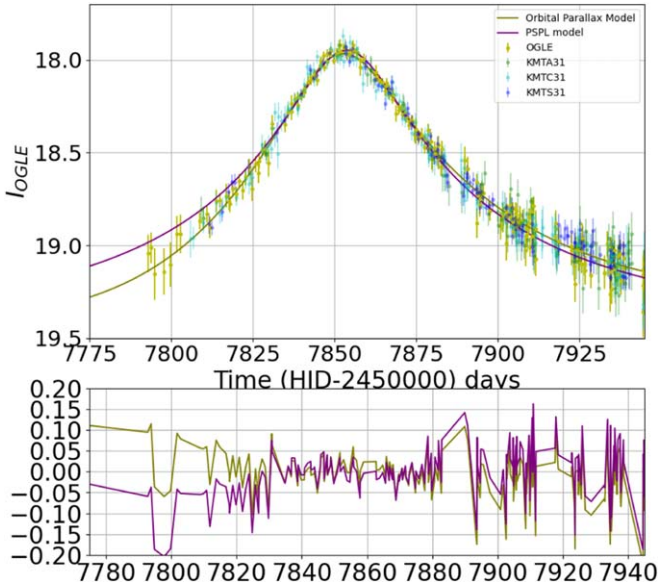
Figure 5. Lightcurve of the event OGLE-2017-BLG-0192.

years for widely spaced pairs. But binary-source microlensing is not sensitive to long-period orbital signatures in the light-curve (S. Rahvar & M. Dominik 2009). Also, given the steepness of the luminosity–mass relation, in most cases, the secondary star might be much fainter than the primary. Consequently, though we might not detect flux from the companion in such cases, the companion may still be able to modulate its trajectory on the lens plane. For this reason, the binarity of the source may sometimes arise just from the perturbation of the motion of the host without any signs of additional light, and the lightcurve can be similar to that of the orbital parallax modulated lightcurve. We, therefore, explore this possibility in the case of both events by analyzing the lightcurve for the

Xallarap effect—"Parallax" spelled backward. The Xallarap vector (ξ_E) is the ratio of the semimajor axis of the source (a_s) normalized to θ_E projected onto the source plane,

$$\xi_E = \frac{a_s}{\theta_E D_s}, \qquad (9)$$

where D_s is the source distance. We form the Xallarap model by introducing seven more parameters: ξ_1 and ξ_2, which are the components of the Xallarap parallel and perpendicular to the source velocity at t_0; i, which is the inclination of the orbital plane i; ϕ_0, which is the phase from the ascending node; ω, which is the angular velocity (day^{-1}); and q_s, which is the mass ratio of the secondary to the primary. We assume circular orbit and a power-law mass–luminosity relation for the main-sequence stars (as can be seen later in the paper) $q_f = q_s^4$, where q_f is the flux ratio (B. W. Carroll & D. A. Ostlie 2017; as can be seen from the result Table 1). We use the *VBBinaryLensing* code originally written in C++ but recently integrated into Python using *pybind*11 (V. Bozza et al. 2021).

We initially model the lightcurves with a single-lens and binary-source Xallarap model. For OGLE-2017-BLG-0103, the χ^2 improves by ~6; for OGLE-2017-BLG-0192, the χ^2 worsens by ~60, but the orbital parameters also do not mimic Earth's orbit. This indicates that the Xallarap model overfits the systematics in the lightcurve of OGLE-2017-BLG-0192, and the event is not affected by the Xallarap effect. But even OGLE-2017-BLG-0103 has only a marginal improvement of χ^2. Therefore, we include orbital parallax in our Xallarap model (now known as the Xallarap+Parallax model) for OGLE-2017-BLG-0103. This further reduces the χ^2 to ~39. So, our Xallarap+Parallax model converges to a solution with a better χ^2 of ~45 than the orbital parallax model. In Figure 6, we verify the authenticity of the Xallarap signal by plotting the cumulative $\Delta\chi^2$ for three models: the Xallarap+Parallax model compared to the parallax model, the Xallarap+Parallax model
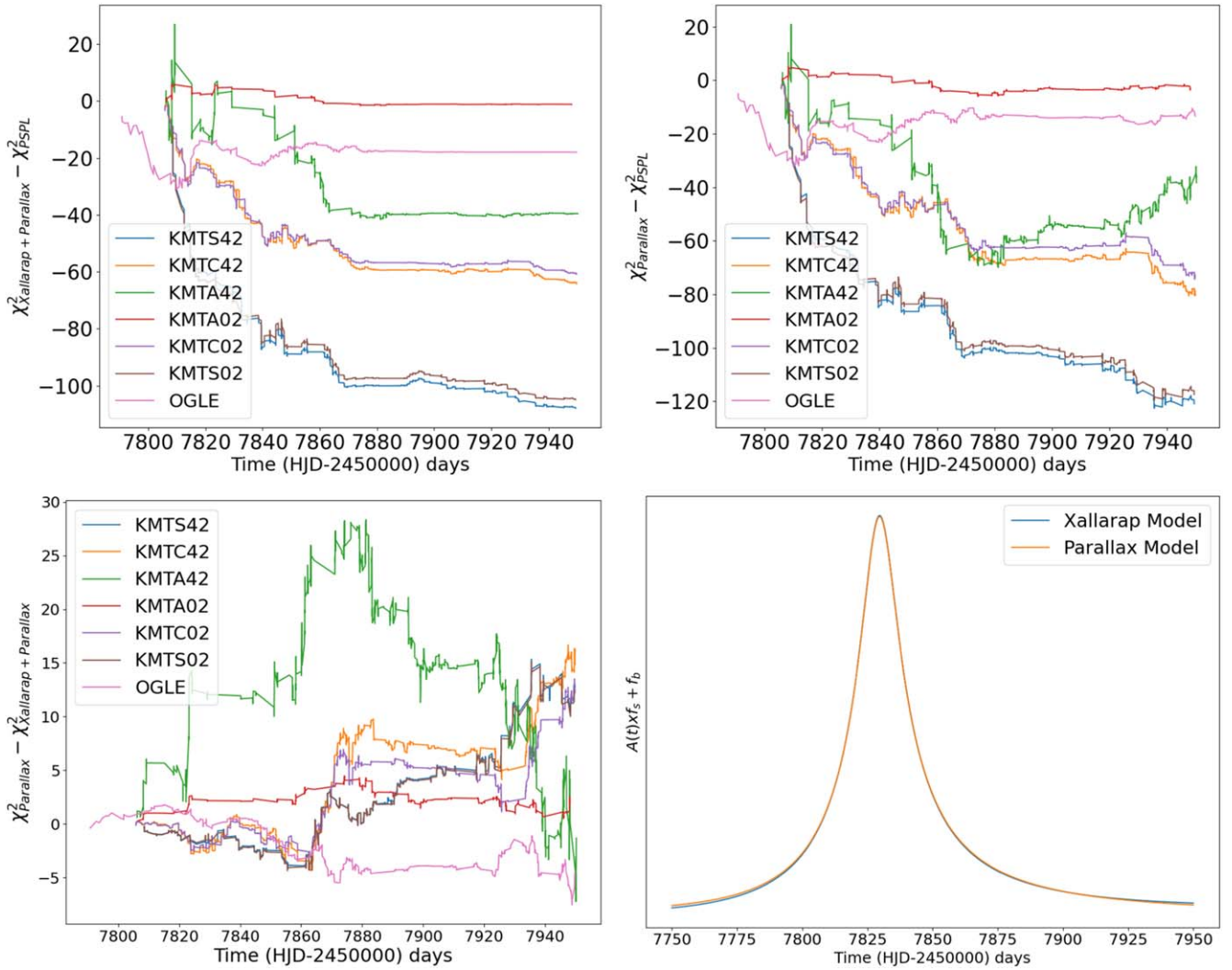
Figure 6. In the figure above, the first three plots show the cumulative sum of the difference in the χ^2 of (a) the Xallarap+Parallax model and the PSPL model, (b) the parallax model and the PSPL model, and (c) Xallarap Model and the PSPL model. The parallax and Xallarap+Parallax models fit better than the PSPL model. We also see that the combined Xallarap+Parallax model shows a marked improvement over the parallax model alone, as indicated by the positive $\Delta\chi^2$ values for most data sets, KMT-A42 in particular. The OGLE data set does not show significant deviation. So, while the parallax model gives a better fit than the PSPL model, adding the Xallarap effect further improves the fit. In the last plot (d), we have shown the Xallarap+Parallax model (blue curve) plotted on top of the parallax model (orange curve).

compared to the PSPL model, and the orbital parallax model compared to the PSPL model. The Parallax and Xallarap+Parallax models fit better than the PSPL model. We also see that the combined Xallarap+Parallax model shows a marked improvement over the parallax model alone, as indicated by the positive $\Delta\chi^2$ values for most data sets, particularly KMT-A42. The OGLE data set does not show significant deviation. So, while the parallax model gives a better fit than the PSPL model, adding the Xallarap effect further improves the fit.

From the model parameters of the event OGLE-2017-BLG-0103 listed in Table 1, we see that the orbital inclination is $\sim 90^{+1.30\circ}_{-0.55}$, the phase angle of the orbit is $\sim 100^{+12.78}_{-9.87}$, and the period of the orbit is $\sim 0.69^{+0.04}_{-0.06}$ yr. The value of the Xallarap vector is $\sim 0.16^{+0.02}_{-0.01}$, and the orbital parallax also converges to a small value, indicating that the Xallarap effect is present in the lightcurve. If we get a Xallarap solution miming the Earth's orbit, the orbital parallax model is favored (S. Rahvar & M. Dominik 2009; S. Miyazaki et al. 2021). However, our results indicate that we are getting a different orbit that does not reflect Earth's orbit projected onto the source plane. The mass

ratio of the source system (q_s) is $0.28^{+0.03}_{-0.03}$, which indicates that the companion is not a planetary object. As these values do not mimic the Earth's orbit, the Xallarap solution cannot be ruled out. We show the lightcurve of OGLE-2017-BLG-0103 and the PSPL, orbital parallax, and Xallarap+Parallax models fitted to it, the residuals plot, the trajectory of the source on the lens plane affected by the best-fit values of π_E and ξ_E, and the covariance plots in Figure 7.

To check whether systematics are playing a role in the Xallarap+Parallax model fit, we performed the autocorrelation analysis of the residuals, e.g., see Figure 8, which shows the autocorrelation versus time plot for the residuals in OGLE data.[3] In all the plots, the autocorrelation function at lag 0 is 1, as expected. The autocorrelation values are close to zero for all other lags and lie within the 95% confidence interval (shaded blue region). This indicates that the residuals do not exhibit significant autocorrelation at any lag, suggesting the absence of systematic trends or correlated noise.

---

[3] The plots for other data sets are shown in Figure 11 in Section 6.
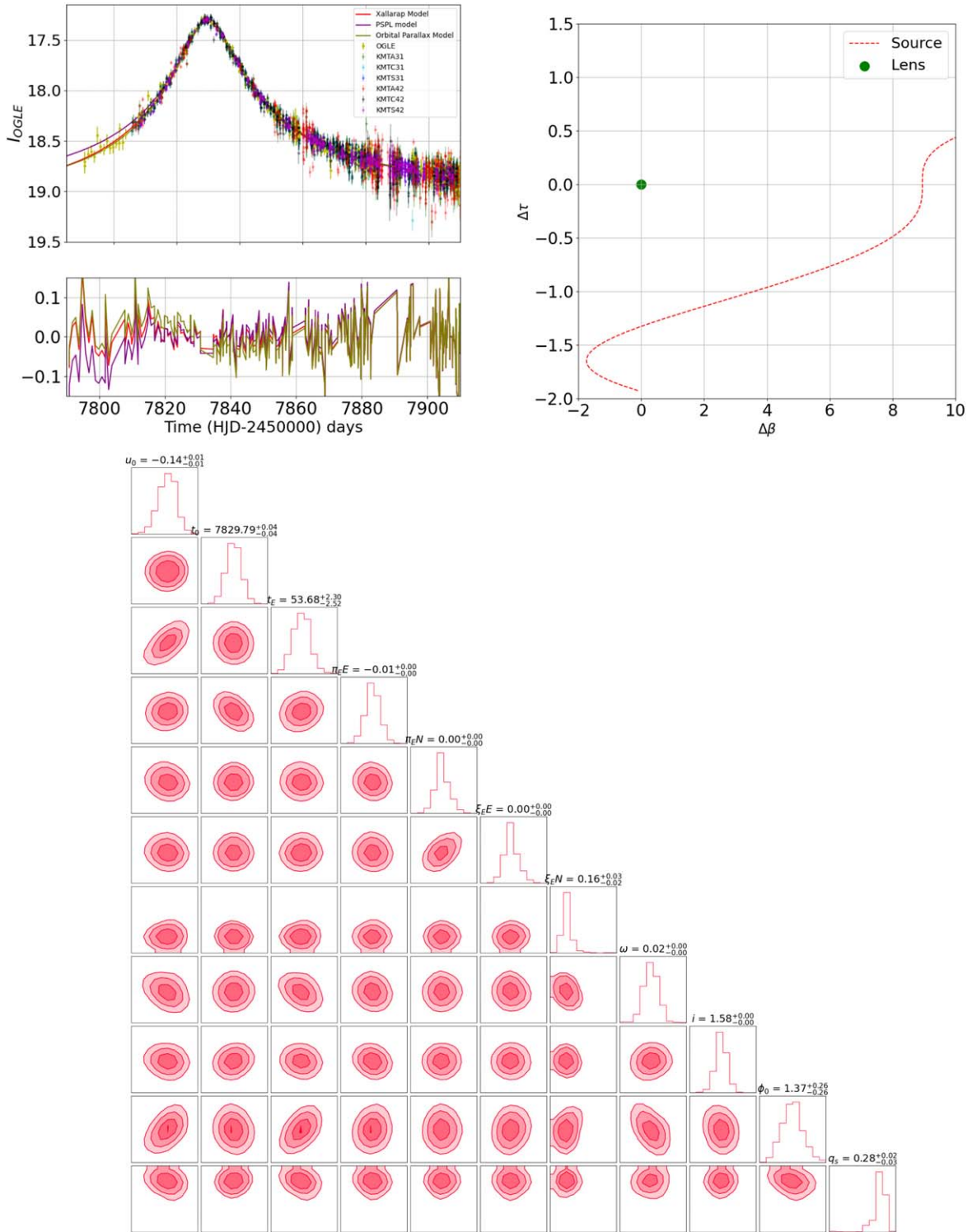
Figure 7. The first plot shows the PSPL, orbital parallax, and Xallarap+Parallax models fitted to the lightcurve of OGLE-2017-BLG-0103. The second plot shows the trajectory of the source system on the lens plane in the Xallarap+Parallax model, and the last plot shows the covariance of the Xallarap+Parallax model parameters. The values of these parameters at 16th, 50th, and 84th quantiles are also given.

4. Color–Magnitude Diagram for OGLE-2017-BLG-0103

We perform the source analysis only for OGLE-20187-BLG-0103 as we find Xallarap signatures in the lightcurve. In the case of OGLE-2017-BLG-0192, we do not show the color–magnitude diagram (CMD) here as there are no Xallarap signatures in the lightcurve. Due to adequate coverage of this OGLE-2017-BLG-0103 by different observatories, the source and blend flux are fairly constrained. We then fit the *V*-band data of the KMTC-BLG42 field to our model and get the values of the source flux and the blend flux in the *V*-band as we got for the *I*-band. We use these fluxes to locate the position of the source and the blend on the CMD formed by the stars in the BLG02 field of the KMTC02 data set (see Figure 9) and find that the source lies on the main sequence. The position of the source and the blend
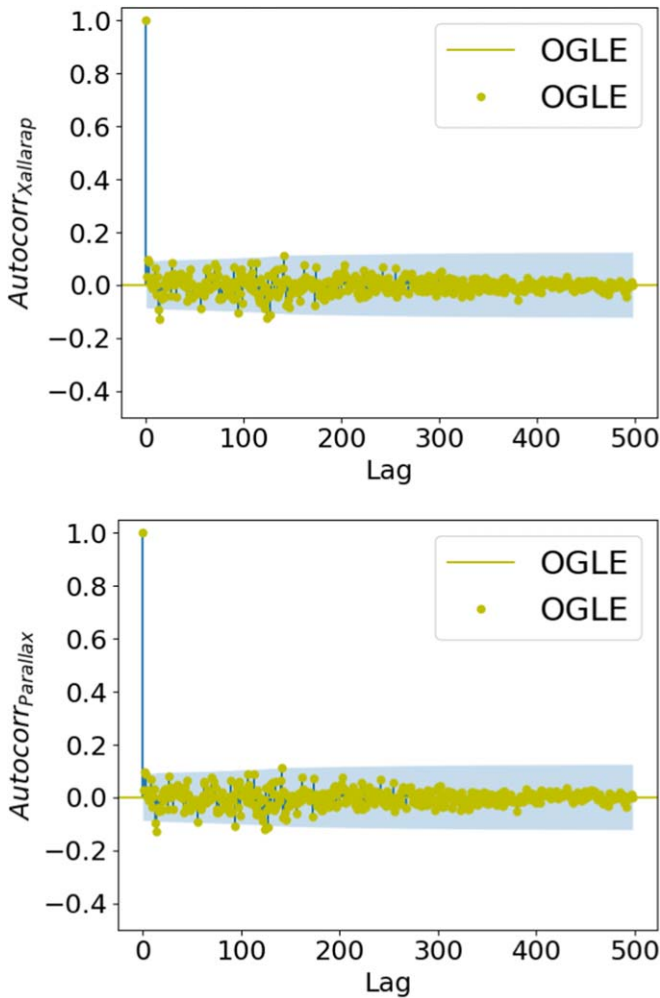
8

Figure 8. Autocorrelation of OGLE.

Figure 9. The CMD of the stars in the field plotted using the V and I band data of KMTC BLG42. The centroid of the Red Clump stars, as estimated by pyDIA, is shown as a red-colored point, while the source and the blend from the lightcurve analysis of OGLE-2017-BLG-0103 are shown in the purple and green colors, respectively.

5. Lens Properties

As mentioned earlier, the modeling of the microlensing lightcurve does not directly give information about the nature of the lens, e.g., its mass and distance, and it can be measured only if θ_E and π_E are measured together from the lightcurve (see Equation (5)). In the case of our events, we do not detect any finite source effects nor have any high-resolution imaging by the Hubble Space Telescope or interferometry observations by VLTI to measure θ_E directly. So, we form a galactic model and simulate the microlensing events that could give rise to measured microlensing model parameters, e.g., t_E and π_E in the case of the orbital parallax model and ξ_E in case of Xallarap +Orbital Parallax model. We formulate the galactic model priors based on the Gaussian velocity distribution toward the bulge (C. Han & A. Gould 1995), the stellar density distribution, and the Chabrier stellar mass function (see G. Chabrier 2003; V. Batista et al. 2011; C. Clanton & B. S. Gaudi 2014; W. Zhu et al. 2017; Y. K. Jung et al. 2018 and others). We assume thin, thick disks with a normalizing factor of 0.12 (M. Jurić et al. 2008; Y. K. Jung et al. 2018). We assume the lens and source distances are free parameters in the galactic model. In addition, we assume certain different conditions to obtain the lens mass and distance using orbital parallax and Xallarap+Parallax models. Since we have obtained the best fit using the orbital parallax model for both events and another possibility using the Xallarap+Parallax model for OGLE-2017-BLG-0103, we discuss our results of the galactic model for both methods separately.

5.1. Physical Properties of the Lens for Both of the Events Using Only the Orbital Parallax Model

Here, we discuss the results using the orbital parallax model. Our galactic model is constrained by the samples of π_E and t_E. Since the source star of OGLE-2017-BLG-0103 has proper-

on the CMD is $((V-I),~I) = ((2.85 \pm 0.04,~19.77 \pm 0.42), (2.43 \pm 0.03,~19.56 \pm 0.46))$, respectively. In the CMD, the centroid of the red-clump stars in the field, the source, and the blend are shown in red, purple, and green colors, respectively. We can see that the source lies on the main sequence, and the blend is located on the bluer side of the CMD but is slightly brighter than the source. We also find the source in the Gaia DR3 database (Gaia Collaboration 2023) with a source ID of 4056392106235284992, source parallax (π_s), equatorial proper motion (μ_{ra}, $\mu_{\delta*}$) = $(-2.10 \pm 0.73$ mas, -8.34 ± 1.11 mas yr^{-1}, and -7.15 ± 0.60 mas yr^{-1}), respectively. The renormalized unit weight error (ruwe) of the source is 1.14, which indicates that the source is a single star or there is no bright companion. The negative value of parallax indicates that the source is faint and heavily blended, which is also evident from the lightcurve and the CMD.

From D. M. Nataf et al. 2013, we find that the intrinsic color of the red clump in the bulge is at $((V-I),~I)_{RC} = (1.06, 14.39)$. On comparing these values with the values for the centroid of the red clump from pyDIA, we estimate the reddening $(\Delta V - I)$ and extinction ΔI toward the BLG02 field as (2.13, 2.10) respectively. This gives the true color and brightness of the source as $((V-I),~I)_{0,s} = (0.71 \pm 0.04, 17.66 \pm 0.42)$.
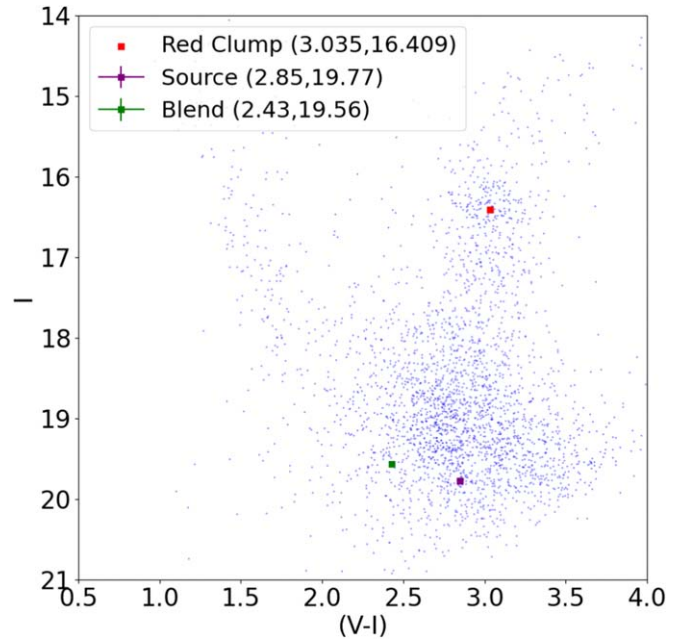
Table 3
The Result Table Shows the Mass of the Lens and the Distance to It for All Four Jerk-Parallax Degenerate Solutions—P1, P2, P3, and P4 of OGLE-2017-BLG-0103 Obtained After Performing the Bayesian Analysis of the Galactic Model

Solution	D_L (kpc)	M_L ($M_\odot$)	D_s (kpc)	$\mu_{\rm rel}$ (mas yr^{-1})	I_L	$M_{s,h}$ ($M_\odot$)	$M_{s,c}$ ($M_\odot$)	a (au)	P (years)
P1	$1.98^{+0.79}_{-0.68}$	$0.21^{+0.23}_{-0.16}$	$7.81^{+0.39}_{-0.31}$	$5.03^{+1.71}_{-1.25}$	$26.48^{+4.38}_{-2.92}$	⋯	⋯	⋯	⋯
P2	$1.61^{+0.79}_{-0.63}$	$0.67^{+0.45}_{-0.23}$	$7.82^{+0.37}_{-0.30}$	$9.16^{+3.22}_{-2.94}$	$18.00^{+4.61}_{-2.68}$	⋯	⋯	⋯	⋯
P3	$1.92^{+0.79}_{-0.63}$	$0.14^{+0.14}_{-0.06}$	$7.81^{+0.38}_{-0.30}$	$4.01^{+0.80}_{-0.71}$	$27.16^{+6.87}_{-3.95}$	⋯	⋯	⋯	⋯
P4	$1.51^{+0.79}_{-0.63}$	$0.70^{+0.24}_{-0.19}$	$7.81^{+0.37}_{-0.30}$	$10.58^{+3.49}_{-3.64}$	$17.70^{+5.18}_{-3.64}$	⋯	⋯	⋯	⋯
Xallarap+Parallax	$7.01^{+0.59}_{-0.68}$	$0.10^{+0.10}_{-0.05}$	8.20	$1.24^{+1.02}_{-0.98}$	$27.82^{+2.93}_{-2.56}$	$1.01^{+0.33}_{-0.25}$	$0.27^{+0.12}_{-0.13}$	$0.98^{+0.14}_{-0.12}$	$0.86^{+0.04}_{-0.06}$

Note. P1 and P3, a pair of solutions, give similar values of M_L and D_L, whereas P2 and P4 give similar values as expected from A. Gould (2004). The brightness in the I band is extinction corrected using Equation (10) and is calculated using the power-law mass–luminosity relation, assuming that the lens is a main-sequence star. The last row shows the galactic model results when the Xallarap+Parallax model is considered.

Table 4
The Result Table Shows the Mass of the Lens, Distance to the Lens, Relative Lens-source Proper Motion, and the Expected Brightness in the I Band of the P1 Solution Obtained for OGLE-2019-BLG-0192, Obtained After Performing the Bayesian Analysis of the Galactic Model

Solution	D_L (pc)	M_L ($M_\odot$)	D_s (pc)	$\mu_{\rm rel}$ (mas yr^{-1})	I_L
P1	$1796.05^{+799.89}_{-686.39}$	$0.10^{+0.21}_{-0.07}$	$7641.87^{+342.58}_{-304.96}$	$1.54^{+0.50}_{-0.39}$	$23.85^{+6.47}_{-5.11}$

Note. The brightness in the I band is calculated using the power-law mass–luminosity relation, assuming that the lens is a main-sequence star.

motion information in Gaia Dr3, we also constrain our galactic model using this information. For this, we transform the proper motion in the galactic plane by referring to the relations by R. Poleski (2013). However, we cannot constrain the galactic model for OGLE-2017-BLG-0192 as the source star has no astrometry information in Gaia Dr3. So, we use only the t_E and π_E information in this event. The results for OGLE-2017-BLG-0103 are given in Table 3 and the results corresponding to the least χ^2 model of OGLE-2017-BLG-0192 in Table 4. These tables also show the lens's proper-motion values and expected brightness (assuming it is a main-sequence star). The expected brightness includes the extinction toward the lens ($A_{I,L}$) computed by using

$$A_{i,L} = \frac{1 - e[-D_L/h_{\rm dust}]}{1 - e[-D_s/h_{\rm dust}]} A_{I,s} \tag{10}$$

where $A_{I,s}$ is the extinction to the source ($=\Delta(I)$ found in the CMD analysis), and $h_{\rm dust}$ is the scale height of the dust toward the line of sight (see D. P. Bennett et al. 2015). From the result table, we see that for OGLE-2017-BLG-0103, the P1 and P3 pair of solutions give similar results of a very low-mass star, having a typical μ_{re} of the disk stars, while the P2 and P4 pair of solutions give similar results where the lens is more massive and has higher $\mu_{\rm rel}$ than the disk stars. The expected brightness of these massive lenses computed assuming they lie on the main sequence is brighter than the blend, which is impossible. This indicates the lens might be a stellar remnant and not a main-sequence star.

5.2. Physical Properties of Lens and Source for OGLE-2017-BLG-0103 Using the Xallarap+Parallax Model

Our Xallarap+Parallax model consists of a single lens but a binary source. We estimate the source's mass (M_s) using MESA Isochrones and Stellar Evolutionary Tracks models (see A. Dotter 2016; J. Choi et al. 2016 for more information)[4] its

color and brightness information (calculated in the Section 4) as $1.28M_\odot$. Thus, using Kepler's third law, we get

$$a = ((M_{sh} + M_{sc})P^2)^{1/3} \tag{11}$$

where $M_s = M_{sh} + M_{sc}$, P is the orbital period, and a is the semimajor axis of the orbit. As we know ω and q_s from our Xallarap+Parallax model, we get $a = 0.98 \pm 0.12$ au, $M_{sh} = 1.01^{+0.1}_{-0.2}\ M_\odot$, and $M_{sc} = 0.27^{+0.04}_{-0.05}\ M_\odot$. Now, ξ_E is related to θ_E by

$$\xi = \frac{1}{\theta_E D_s} P^{2/3} \frac{(q_s M_{s,h}^{1/3})}{(1 + q_s)^{2/3}}. \tag{12}$$

Thus, we get $\theta_E = 0.16 \pm 0.04$ mas. Using the galactic model, we can constrain the mass of the lens and distance to it. In our galactic model analysis using the Xallarap+Parallax model, we keep M_L and D_L as free parameters such that D_L is always less than D_s. We use I_b as the upper limit on the lens brightness, assuming that the lens is also a main-sequence star. Since π_E converges to a very small value in the Xallarap+Parallax model, we ignore the parallax constraint.[5] Instead, we use Equation (12). We use the other priors similar to the ones used in the previous galactic model analysis using the orbital parallax model. We show the distribution of M_L and D_L in Figure 10. Interestingly, as the Xallarap is more sensitive to the lenses closer to the source (M. Dominik 1998), the lens moves further and is closer to the source this time than in the earlier galactic model analysis.

The physical parameters are listed in the last row of Table 3.

6. Discussion

In this study, we have analyzed two microlensing events, OGLE-2017-BLG-0103 and OGLE-2017-BLG-0192, to try to identify the nature of the microlens and source. These events peaked close to the vernal equinox in 2017 when the jerk velocity (v_j) and the projected acceleration of the Sun (α) were

---

[4] Also visit http://waps.cfa.harvard.edu/MIST/index.html to access the database and various tools.

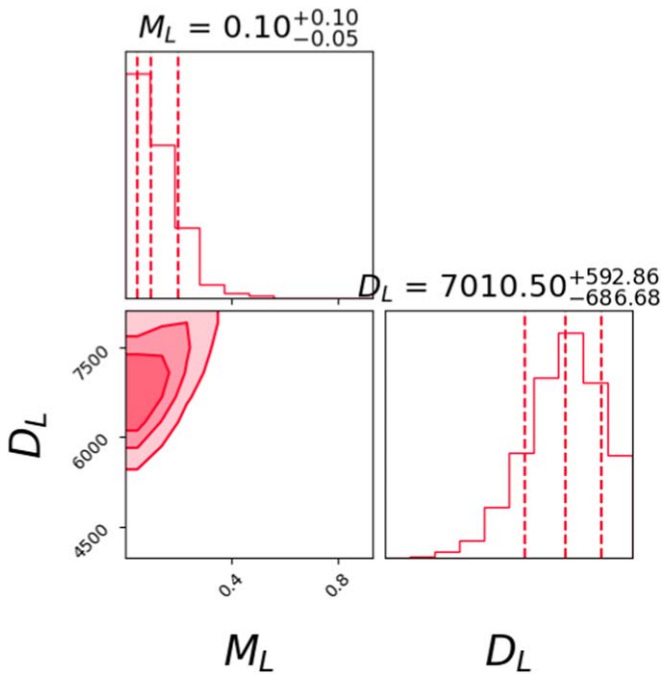[5] We also do not use Equation (5) as it will lead to a massive lens.

Figure 10. The posterior distributions of M_L ($M_\odot$), and D_L (kpc) shown at 16th, 50th, and 84th percentile levels.

very high. This introduces a Jerk-Parallax degeneracy in events with t_E less than 60 days. While this degeneracy is manifested as continuous contours in the π_E plane, for events with slightly longer t_E and a higher value of α, the degeneracy is converted to a discrete degeneracy (e.g., OGLE-2017-BLG-0103). For even larger t_E, we find that the high value of α and t_E splits the π_E contours, and the degeneracy is resolved (e.g., OGLE-2017-BLG-0192).

For OGLE-2017-BLG-0103, while we find that orbital parallax is responsible for the asymmetry in the lightcurve, we also find that the Xallarap effect added to the orbital parallax model also explains the asymmetry with an improved $\Delta\chi^2$ of ~45. The source orbital parameters do not reflect the Earth's orbit, indicating that the model does not reflect Earth's orbit on the source plane. When plotted, the cumulative distribution of χ^2_{Parallax} - $\chi^2_{\text{Xallarap+Parallax}}$ plots shows an increasing trend indicating that the Xallarap signal is present throughout the lightcurve and is improving the fit. As another quality check, we plotted the autocorrelation of the residuals of the Xallarap+Parallax model at various lags of all the data sets. We found that the correlation of the data is much less, thereby indicating no influence of the systematic trend in the data on the fitted model. This indicates severe tension in both the orbital parallax and Xarallarap+Parallax models.

Previous works by M. Dominik (1998), M. C. Smith et al. (2003), M. C. Smith (2003), S. Rahvar & M. Dominik (2009), and S. Miyazaki et al. (2021) have shown that the Xallarap signal is prominent for super-Jupiter mass planets in close orbits. This signal increases with the mass, and the wiggles in the lightcurve are most visible when the orbital period is small, and the planet's mass is higher (see S. Rahvar & M. Dominik 2009; S. Miyazaki et al. 2021). In the case of OGLE-2017-BLG-0103, the companion is stellar, and the orbital period is ~0.8 yr; hence, we see an asymmetry in the lightcurve instead of wiggles. Such events are expected to be common during the Nancy Grace

Roman Space Telescope era (D. Spergel et al. 2015), which was previously named WFIRST (see D. P. Bennett et al. 2018; B. S. Gaudi et al. 2019; M. T. Penny et al. 2019).

To derive the source properties, we obtained each data set's source and the blend fluxes by performing the linear regression of the microlensing model to the data. We use the V-band data of KMTC02 to plot the CMD and then locate the position of the source and the blend on the CMD. The blend is bluer and slightly brighter than the source. Based on its position on the color–magnitude diagram (CMD), we find that the source is a main-sequence star.

Given the inherent limitations of the microlensing lightcurve of both events, which hinder the direct measurement of finite-source effects and, consequently, the Einstein radius (θ_E), we turned to a galactic model analysis to estimate the mass and distance of the lens. For OGLE-2017-BLG-0192, the galactic model analysis constrained by the samples of t_E and π_E of the best-fitted P1 solution gives $M_L \sim 0.1$ $M_\odot$ and located in the near disk. Assuming that the lens is a main-sequence star, we find that it is very faint ($I_L = 24$ mag). For OGLE-2017-BLG-0103, we did two separate analyses for the orbital parallax and Xallarap+Parallax models. The galactic model for OGLE-2017-BLG-0192 was constrained only by the samples of t_E and π_E. However, the galactic model for OGLE-2017-BLG-0103 was constrained not only by the samples of t_E and ξ_E, but also the source proper-motion (μ_s) information from Gaia Dr3. The orbital parallax model gives us two similar solutions: one gives a very low-mass main-sequence star in the disk, and the other gives a more massive star that is nearer than the former.[6] Assuming again that the lens is a main-sequence star, the expected I-band brightness of the lens for the former pair of solutions is >25 mag, while it is ~18 mag in the case of the latter. If the latter pair of solutions are correct, then this will imply that the lens is itself the blend and the lens-source pair can be observed using high-resolution telescopes by the year 2027 (considering the proper-motion values given in Table 3).

The galactic model analysis using the Xallarap+Parallax model shows that the lens is an $\sim 0.1 M_\odot$ dwarf star in the galactic bulge. As expected, our galactic model, constrained by the Xallarap signal in the lightcurve, moves the lens further than the galactic model constrained by only orbital parallax. In our galactic model analysis, we have assumed the source to be located in the bulge at the distance of 8.2 kpc. Using MESA isochrone models, we find that the source host has a mass $\sim 1.01 M_\odot$ and it is orbited by an $\sim 0.27 M_\odot$ dwarf star at a separation of ~ 0.98 au and has an orbital period of ~ 0.8 yr.

Finally, the question arises: which model is true? Degeneracies are difficult to break in the case of single-lens events due to the symmetry in the magnification pattern around the point caustic of the lens. If we apply Ocazm's razor to the event OGLE-2017-BLG-0103, the orbital parallax model is most likely as it is explained by fewer bodies and a smaller number of parameters. However, the degenerate pairs of orbital parallax solutions also have different lens properties. S. Rahvar & M. Dominik (2009) state that a $\Delta\chi^2 \geqslant 11.09$ is necessary to claim a Xallarap detection. In our case, we have a $\Delta\chi^2$ of ~45. Moreover, combined orbital parallax and Xallarap signals show an increasing trend in the cumulative distribution of the $\Delta\chi^2$ than only the orbital parallax signal. We also do not find any

---

[6] as predicted by (A. Gould 2004), both pairs of Jerk-Parallax solutions give different properties for the lens.
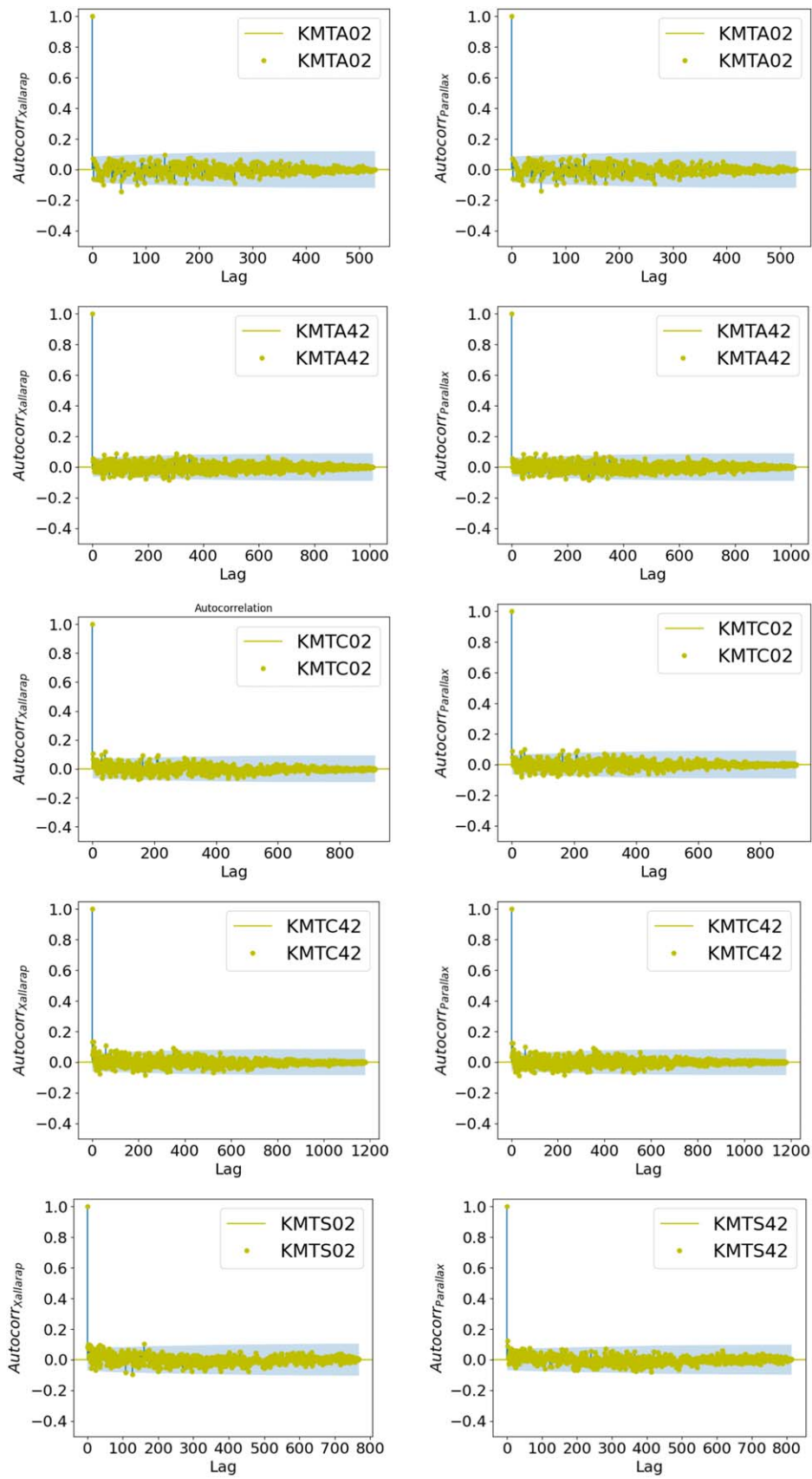
Figure 11. Autocorrelation plots for different data sets. The autocorrelation is computed for the residuals of the best-fitted Xallarap+Parallax model for the lightcurve of OGLE-2017-BLG-0103.

influence from systematics. Indeed, for many microlensing events of interest, models with Xallarap may compete with models with Parallax and cannot be excluded easily (e.g., see N. Miyake et al. 2012; N. Koshimoto et al. 2017; P. Rota et al. 2021; Y. K. Satoh et al. 2023). The Xallarap+Parallax model could be ruled out if the source has a mass incompatible with the observed flux in follow-up imaging (A. Bhattacharya et al. 2017, 2020; J. W. Blackman et al. 2021). Furthermore, during lightcurve fitting, if a Xallarap+Parallax model returns an orbital period of 1 yr, there is a high chance that the fit has converged to a mirror solution of a parallax model (S. Dong et al. 2009; K. -H. Hwang et al. 2011) and then the Xallarap+Parallax model can be discarded. But this is not the case with our model. Also, assuming that the lens is also a main-sequence star, we are finding the brightness of the lens consistent with the blend and source position on the CMD. So, it is difficult to rule out the Xallarap+Parallax model easily. It also is to be noted that all the studies that were previously published using the Xallarap analysis to date are binary-lens events and this is the first study using a single-lens model.

In this study, we assume that the lens is single because the lightcurve resembles a Paczynski curve. If a binary lens would have to produce a similar signal, then assuming the orbital period of ~0.8 yr and the mass of the lens as $0.1 M_\odot$, this would imply a separation (s) of 0.4 au between the lens components. At such a separation, the line caustic formed by a lower-mass companion would not go undetected in the lightcurve. Computing the magnification of a binary lens requires four additional parameters: s, ϕ, the mass ratio of the lens q, and ρ. It also requires solving fifth-order complex polynomials for every pair of s and q in the parameter space. In addition, parameters $\dot{s}$ and $\dot{\phi}$ also enter the parameter list when the orbital motion of the lens effect is added to the modeling. Assuming a trajectory angle (ϕ) such that the source goes away from the caustic structure would imply a single-lens event. Then, involving a secondary lens becomes unnecessary. So, in this work, we have not modeled the lightcurves using a binary lens with an orbital motion effect.

We can expect many such events using the Nancy Grace Roman Space Telescope mission. While most of the focus of the microlensing community today is to analyze binary or tertiary events, single-lens events with asymmetric lightcurves need attention to find hidden signatures like OGLE-2017-BLG-0103. It is difficult to address any Xallarap solution as the source is faint, cannot be resolved using the current survey telescopes, and is usually in the bulge. So, a program for future AO observations using powerful large aperture telescopes like the Thirty Meter Telescope (G. H. Sanders 2013; W. Skidmore et al. 2015) can be made to study the degenerate solutions. Such observations can potentially validate the lens's mass and distance obtained using the galactic model constrained by various microlensing parameters.

Appendix
Autocorrelation Results of Xallarap and Parallax Models

In this section, we show the autocorrelation of the residuals calculated for the whole duration of the lightcurve for the KMTNet data set. The residuals are the difference between the Xallarap+Parallax model and the observed data. The autocorrelation is 1 at lag 0, which is expected. However, as the lag value increases, the autocorrelation values for all the data sets drop and are consistently close to zero and within the 95% confidence interval throughout.

ORCID iDs

Sarang Shah ⬤ https://orcid.org/0000-0003-1959-8439

References

Alard, C., & Lupton, R. H. 1998, ApJ, 503, 325
Albrow 2017, MichaelDAlbrow/pyDIA: Initial release on github, Zenodo, doi:10.5281/zenodo.268049
Alcock, C., Akerlof, C.~W., Allsman, R.~A., et al. 1993, Natur, 365, 621
Alcock, C., Allsman, R. A., Alves, D., et al. 1995a, ApJL, 454, L125
Alcock, C., Allsman, R. A., Axelrod, T. S., et al. 1995b, ApJ, 445, 133
An, J. H., Albrow, M. D., Beaulieu, J.-., et al. 2002, ApJ, 572, 521
Aubourg, E., Bareyre, P., Bréhin, S., et al. 1993, Natur, 365, 623
Bagheri, F., Sajadian, S., & Rahvar, S. 2019, MNRAS, 490, 1581
Batista, V., Gould, A., Dieters, S., et al. 2011, A&A, 529, A102
Bennett, D. P., Akeson, R., Anderson, J., et al. 2018, arXiv:1803.08564
Bennett, D. P., Becker, A. C., Calitz, J. J., et al. 2002a, arXiv:astro-ph/0207006
Bennett, D. P., Becker, A. C., Quinn, J. L., et al. 2002b, ApJ, 579, 639
Bennett, D. P., Bhattacharya, A., Anderson, J., et al. 2015, ApJ, 808, 169
Bhattacharya, A., Bennett, D. P., Anderson, J., et al. 2017, ApJ, 154, 59
Bhattacharya, A., Bennett, D. P., Beaulieu, J. P., et al. 2020, arXiv:2009.02329
Blackman, J. W., Beaulieu, J. P., Cole, A. A., et al. 2021, AJ, 161, 279
Bond, I. A., Abe, F., Dodd, R. J., et al. 2001, MNRAS, 327, 868
Bond, I. A., Abe, F., Dodd, R. J., et al. 2002, MNRAS, 331, L19
Bozza, V., Khalouei, E., & Bachelet, E. 2021, MNRAS, 505, 126
Bramich, D. M., Horne, K., Albrow, M. D., et al. 2013, MNRAS, 428, 2275
Carroll, B. W., & Ostlie, D. A. 2017, An Introduction to Modern Astrophysics (2nd ed.; Cambridge: Cambridge Univ. Press)
Chabrier, G. 2003, pasp, 115, 763
Choi, J., Dotter, A., Conroy, C., et al. 2016, ApJ, 823, 102
Clanton, C., & Gaudi, B. S. 2014, ApJ, 791, 91
Delplancke, F., Górski, K. M., & Richichi, A. 2001, A&A, 375, 701
Dominik, M. 1998, A&A, 329, 361
Dong, S., Gould, A., Udalski, A., et al. 2009, ApJ, 695, 970
Dong, S., Mérand, A., Delplancke-Ströbele, F., et al. 2019, ApJ, 871, 70
Dotter, A. 2016, ApJS, 222, 8
Einstein, A. 1936, Sci, 84, 506
Foreman-Mackey, D., Hogg, D. W., Lang, D., & Goodman, J. 2013, PASP, 125, 306
Gaia Collaboration, Vallenari, A., Brown, A. G. A., et al. 2023, A&A, 674, A1
Gaudi, B. S., Akeson, R., Anderson, J., et al. 2019, BAAS, 51, 211
Gould, A. 1992, ApJ, 392, 442
Gould, A. 1994, ApJL, 421, L71
Gould, A. 2004, ApJ, 606, 319
Gould, A., Miralda-Escude, J., & Bahcall, J. N. 1994, ApJL, 423, L105
Gould, A., Udalski, A., Monard, B., et al. 2009, ApJL, 698, L147
Griest, K., & Hu, W. 1992, ApJ, 397, 362
Han, C., & Gould, A. 1995, ApJ, 447, 53
Han, C., & Gould, A. 1997, ApJ, 480, 196
Hog, E., Novikov, I. D., & Polnarev, A. G. 1995, A&A, 294, 287
Hwang, K.-H., Han, C., Udalski, A., et al. 2011, MNRAS, 413, 1244
Jiang, G., DePoy, D. L., Gal-Yam, A., et al. 2004, ApJ, 617, 1307
Jung, Y. K., Hwang, K.-H., Ryu, Y.-H., et al. 2018, ApJ, 156, 208
Jurić, M., Ivezić, Ž, Brooks, A., et al. 2008, ApJ, 673, 864

Kim, H.-W., Hwang, K.-H., Shvartzvald, Y., et al. 2018, arXiv:1806.07545
Kim, S.-L., Lee, C.-U., Park, B.-G., et al. 2016, JKAS, 49, 37
Koshimoto, N., Udalski, A., Beaulieu, J. P., et al. 2017, ApJ, 153, 1
Mao, S., Smith, M. C., Wozniak, P., et al. 2002, MNRAS, 329, 349
Miyake, N., Udalski, A., Sumi, T., et al. 2012, ApJ, 752, 82
Miyazaki, S., Johnson, S. A., Sumi, T., et al. 2021, AJ, 161, 84
Nataf, D. M., Gould, A., Fouque, P., et al. 2013, ApJ, 769, 88
Nemiroff, R. J., & Wickramasinghe, W. A. D. T. 1994, ApJL, 424, L21
Paczynski, B. 1986, ApJ, 304, 1
Paczynski, B. 1997, arXiv:astro-ph/9711007
Park, B.-G., DePoy, D. L., Gaudi, B. S., et al. 2004, ApJ, 609, 166
Penny, M. T., Gaudi, B. S., Kerins, E., et al. 2019, ApJS, 241, 3
Poindexter, S., Afonso, C., Bennett, D. P., et al. 2005, ApJ, 633, 914
Poleski, R. 2013, arXiv:1306.2945
Rahvar, S., & Dominik, M. 2009, MNRAS, 392, 1193
Rota, P., Hirao, Y., Bozza, V., et al. 2021, AJ, 162, 59

Sahu, K. C., Anderson, J., Casertano, S., et al. 2022, ApJ, 933, 83
Sanders, G. H. 2013, JApA, 34, 81
Satoh, Y. K., Koshimoto, N., Bennett, D. P., et al. 2023, AJ, 166, 116
Skidmore, W. & TMT International Science Development Teams 2015, RAA, 15, 194512
Skowron, J., Udalski, A., Gould, A., et al. 2011, ApJ, 738, 87
Smith, M. C. 2003, MNRAS, 343, 1172
Smith, M. C., Mao, S., & Paczyński, B. 2003, MNRAS, 339, 925
Soszynski, I., Zebrun, K., Wozniak, P. R., et al. 2001, ApJ, 552, 731
Spergel, D., Gehrels, N., Baltay, C., et al. 2015, arXiv:1503.03757
Sumi, T., Abe, F., Bond, I. A., et al. 2003, ApJ, 591, 204
Udalski, A., Szymanski, M., Kaluzny, J., et al. 1994, AcA, 44, 1
Udalski, A., Szymański, M. K., & Szymański, G. 2015, Ac, 65, 1,
Witt, H. J., & Mao, S. 1995, ApJL, 447, L105
Yoo, J., DePoy, D. L., Gal-Yam, A., et al. 2004, ApJ, 603, 139
Zhu, W., Udalski, A., Calchi Novati, S., et al. 2017, ApJ, 154, 210